Contents lists available at ScienceDirect

Applied Catalysis B: Environment and Energy

Phosphate-supported palladium single atom and nanoparticle boost ambient temperature tandem hydrogenolysis–hydrogenation of furan alcohols/aldehydes

Jialuo Lu [a,1], Yong Liu [b,1], Jun Wang [a], Zheling Zeng [a], Lungang Chen [c], Shuguang Deng [d], Ji-Jun Zou [e], Qiang Deng [a,*]

[a] School of Chemical and Chemical Engineering, Nanchang University, No. 999 Xuefu Avenue, Nanchang 330031, PR China
[b] School of Resources and Environment, Key Laboratory of Poyang Lake Environment and Resource Utilization, Ministry of Education, Nanchang University, No. 999 Xuefu Avenue, Nanchang 330031, PR China
[c] School of Energy and Environment, Key Laboratory of Energy Thermal Conversion and Control of Ministry of Education, Southeast University, No. 2 Sipailou, Nanjing 210096, PR China
[d] School for Engineering of Matter, Transport and Energy, Arizona State University, 551 E. Tyler Mall, Tempe, AZ 85287, USA
[e] School of Chemical Engineering and Technology, Tianjin University, No.92 Weijin Road, Tianjin 300072, PR China

ARTICLE INFO

ABSTRACT

Developing a one-pot method for tandem hydrogenolysis–hydrogenation of biomass-derived furan-based alcohols to methyltetrahydrofurans is challenging but crucial for synthesizing sustainable biofuels and chemicals. Herein, we report the efficient hydrogenolysis–hydrogenation of furan alcohol to 2-methyltetrahydrofuran using a phosphate-supported synergistic palladium single atom and nanoparticle at an ambient temperature. Comprehensive characterizations and theoretical calculations reveal that in situ H$_2$ heterolysis at the palladium single atom–AlPO$_4$ interface generates frustrated Lewis H$^+$–H$^-$ pairs, which selectively cleaves the C–OH bond in furan alcohol to form 2-methylfuran, and H atoms on the palladium nanoparticle surface promotes the subsequent C=C hydrogenation of 2-methylfuran to 2-methyltetrahydrofuran. Additionally, the catalyst shows generality for various furan and heterocyclic alcohols. Furthermore, the catalyst exhibits excellent activity in the hydrogenation–hydrogenolysis–hydrogenation of furan aldehydes to methyltetrahydrofurans. The results provide a highly efficient reaction for synthesizing methyltetrahydrofurans at ambient temperature, which has excellent potential for industrial applications.

1. Introduction

Catalytic conversion of furan alcohols (e.g., furan alcohol, 5-methyl-furan alcohol, and 2,5-dihydroxymethyl furan) and furan aldehydes (e.g., furfural, 5-methylfurfural, and 5-hydroxymethylfurfural) to biofuels and fine chemicals represents an excellent opportunity for mitigating carbon footprint and developing a green economy [1–3]. Because of their high energy densities, octane numbers, and boiling points, methyltetrahydrofurans (e.g., 2-methyltetrahydrofuran and 2,5-dimethyltetrahydrofuran) are important high-value chemicals that can not only be used as biofuels but also as aprotic ether solvents in various organic reactions [4]. Although the synthesis of methyltetrahydrofurans from furan alcohols/aldehydes can be theoretically achieved with a high yield

via a two-pot method comprising the hydrogenolysis of alcohols/aldehydes to intermediate methylfurans (e.g., 2-methylfuran and 2,5-dimethylfuran) and subsequent hydrogenation of methylfurans to methyltetrahydrofurans [5–10], the isolation and recovery of methyl-furan intermediates prior to hydrogenation remains a pressing issue for establishing a greener synthesis route. Therefore, the development of an upgraded one-pot method for converting furan alcohols/aldehydes into methyltetrahydrofurans with higher energy integration and production efficiency is highly desirable.

Generally, the hydrogenolysis of furan alcohols is a metal–acid bifunctionally catalyzed reaction, in which the metallic and acidic sites activate H$_2$ and the C–OH bond, respectively, whereas the hydrogenation of methylfurans is a common metal-catalyzed reaction. In early

---

* Corresponding author.
 E-mail address: dengqiang@ncu.edu.cn (Q. Deng).
[1] These authors contributed equally to this work.

studies, a two-step method was developed wherein furan alcohols/aldehydes were hydrogenolyzed in the range 170 °C–240 °C over bifunctional catalysts (e.g., $CuCr_2O_4$, Co/Al_2O_3, and $Cu_2Si_2O_5(OH)_2$), and intermediate methylfurans were subsequently hydrogenated in the range 170 °C–300 °C over hydrogenation catalysts (e.g., Pd/C, Ni/SiO_2, and Pd/SiO_2) to produce an overall yield of approximately 80% methyltetrahydrofurans [11–13]. Unfortunately, two-step reactions employ high temperatures, multiple apparatus, and prolonged reaction times. Subsequently, several metal-supported solid acid (e.g., Cu–Ni–Re/Hβ, $PdCu/ZrO_2$, $Cu–Ni/TiO_2$, and $IrIrO_x/C$) have been used for one-pot syntheses in the range 220 °C–240 °C [14–17]. However, in these simply supported bifunctional catalysts, metallic and acidic sites are spatially separated [8,18,19], and the weakly synergistic catalysis often leads to inferior C–OH hydrogenolysis activity and selectivity. Meanwhile, at the catalyst's metallic sites, the competitive adsorption of various furan-based reactant intermediates (e.g., furan aldehydes/alcohols) results in a low activity for hydrogenating methylfurans. Therefore, the reaction usually requires an elevated temperature and predominantly generates some unwanted tetrahydrofuran alcohols (e.g., tetrahydrofuran alcohol, 5-methyltetrahydrofuran alcohol, and 2, 5-dihydroxymethyltetrahydrofuran) via the parallel furan hydrogenation side reaction, which cannot be hydrogenolyzed to targeted methyltetrahydrofurans [12–17]. More importantly, in most studies, the main products focused on furfural/furan alcohol-based 2-methyltetrahydrofurans, 5-methyl furfural/5-methylfuran alcohol and 5-hydroxymethyl furfural/2,5-dihydroxymethyl furan-derived 2, 5-dimethyltetrahydrofuran have scarcely been reported to date, which suggests that the regulation of the desired tandem route via the initial hydrogenolysis and subsequent hydrogenation under mild reaction conditions while simultaneously maintaining an excellent catalytic generality is very challenging.

Herein, a series of phosphate-supported palladium single atom and nanoparticle ($Pd_{1+NP}/AlPO_4$, Pd_{1+NP}/BPO_4, $Pd_{1+NP}/Al(PO_3)_3$, and $Pd_{1+NP}/Y(PO_3)_3$) containing abundant Pd–phosphate interfaces and rich bare Pd surfaces was fabricated for the tandem hydrogenolysis–hydrogenation of furan alcohols/aldehydes to methyltetrahydrofurans. The catalytic mechanism suggests that at the Pd–phosphate interface, the frustrated Lewis-acid pair Pd–O–P, can generate asymmetric hydrogen pairs $H^-–Pd…(OH^+)P$ via an interesting H_2 heterolysis mechanism. The $H^+–H^-$ pairs generated in situ can facilitate the adsorption of the asymmetric C–OH moiety and hinder the activation of the furan moiety in furan alcohols, which enables the highly selective C–OH hydrogenolysis and simultaneously inhibits the parallel C═C hydrogenation. Subsequently, Pd nanoparticles promote the hydrogenation of methylfurans to methyltetrahydrofurans. At 30 °C, furan alcohol can be completely converted, and a methyltetrahydrofuran selectivity of 83.3% was achieved over $Pd_{1+NP}/AlPO_4$, which represents an unprecedented catalytic activity, especially at ambient temperature. The active site was clearly identified based on a detailed comparative study using pure phosphate-supported Pd single atom and phosphate-supported Pd nanoparticle catalysts. The ambient-temperature hydrogenolysis–hydrogenation strategy shows excellent universality and extensibility for various furan-based and heterocyclic alcohols. In addition, the powerful multifunctional catalyst enables the highly efficient conversion of furan aldehydes to methyltetrahydrofurans via successive hydrogenation, hydrogenolysis, and hydrogenation route. During recycling, the catalyst showed excellent stability, while neither the activity nor selectivity degraded. Thus, the catalyst shows excellent industrial application potential for controllably synthesizing methyltetrahydrofurans via the cooperative catalysis of Pd single atoms and nanoparticles.

2. Materials and methods

2.1. Preparation of Pd1 +NP-supported phosphate

Pd_{1+NP}-supported phosphates were prepared by a simple incipient wetness impregnation method. Typically, 0.042 g of $Pd(NH_3)_4(NO_3)_2$ was added to a mixture of 0.30 g of supports (i.e., $AlPO_4$, $Al(PO_3)_3$, BPO_4, $Y(PO_3)_3$), two drops of dilute hydrochloric acid (2 mol·L^{-1}), and 10 mL of water, followed by heating at 80 °C to thoroughly evaporate the water and reach a theoretical Pd loading of 5.0 wt%. The Pd_{1+NP}-based catalysts were obtained by calcination at 400 °C for 2 h under a static air atmosphere and reduction at 50 °C for 2 h in a 10% H_2/Ar atmosphere.

2.2. Preparation of Pd1-supported phosphate

Pd_1-supported phosphate was prepared by an incipient impregnation method. Typically, 0.004 g of $Pd(NH_3)_4(NO_3)_2$ was added to a mixture of 0.30 g of $AlPO_4$, two drops of dilute hydrochloric acid (2 mol·L^{-1}), and 10 mL of water, followed by heating at 40 °C and stirring for 3 h. Then, $Pd_1/AlPO_4$ was obtained by filtration, washed by water, and drying at 100 °C for 12 h in vacuum, and calcination at 400 °C for 2 h under a static air atmosphere and reduction at 50 °C for 2 h in a 10% H_2/Ar atmosphere.

2.3. Preparation of PdNP-supported phosphate

Pd_{NP}-supported phosphate was prepared by a pre-reduction of $PdCl_2$ to Pd nanoparticle and subsequent incipient wetness impregnation method. Briefly, 5 mL $NaBH_4$ aqueous solution (0.13 mol·L^{-1}) was slowly added to the mixture of 0.0256 g of $PdCl_2$ and 10 mL of water under vigorous stirring for 1 h, and Pd nanoparticles were obtained after centrifugation, washed by water, and drying at 150 °C in vacuum. $AlPO_4$ supported catalyst was prepared by mixing of 0.3 g of $AlPO_4$, 0.015 g of Pd nanoparticles (with 5.0 wt% Pd loading), and 20 mL of ethanol for 10 min, heating at 80 °C to thoroughly evaporate ethanol, washing with H_2O and drying at 150 °C in vacuum. The Pd_{NP}-based catalysts were obtained by calcination at 400 °C for 2 h under a static air atmosphere and reduction at 50 °C for 2 h in a 10% H_2/Ar atmosphere.

2.4. Characterization methods

Various testing methods, including DRIFT, N_2 adsorption/desorption, ICP-OES, HR-TEM, EDS mapping, HAADF-STEM, XPS, FTIR, in situ NAP-XPS, Solid-state ^{31}P NMR, Py-FTIR, UV-Vis, and catalytic kinetic analysis and calculation models were adopted to measure the physicochemical properties and reaction mechanism. The detailed measuring processes are provided in the Supplementary Information.

2.5. Catalytic reactions

The hydrogenation-hydrogenolysis reaction was conducted in a 25 mL batch autoclave equipped with a mechanical stirrer (NST25-P5-T3-SS1-R, Anhui Kemi Machinery Technology Co., LTD). Briefly, 0.1 mmol of furan alcohols, 10 mL of tetrahydrofuran, and 0.05 g of $Pd_{1+NP}/AlPO_4$ or 0.035 g of $Pd_{NP}/AlPO_4$ or 0.115 g of $Pd_1/AlPO_4$ with identical Pd^0 or Pd^{2+} content were added into the reactor under the string. Before the reaction, the air in the reactor was replaced with hydrogen several times. Then, the mixture was heated to 30 °C under 4.0 MPa H_2 pressure, and periodically sampled with 0.5 mL after reaching the target reaction time. Subsequently, 1 mL of ethyl acetate was used to extract organics, and 10 μL of *N,N*-dimethylformamide was used as an internal standard substance. The reaction mixture was qualitatively analyzed by an Agilent 6890 N GC/5973 MS detector and quantitatively analyzed by a Trace 1300 gas chromatograph equipped with a TG-WAXMS capillary column (30 m × 0.32 mm). The carbon loss during the reaction is

attributed to the formation of humins. The reported data were the mean values of three trials with small error bars.

2.6. Density functional theory calculation

The details about the theoretical calculation method can be found in the Supplementary Information.

3. Results and discussion

3.1. Structural characterization of phosphate-based catalysts

Pd single atom-dispersed aluminum phosphate ($Pd_1/AlPO_4$) was prepared via a simple incipient method by combining $Pd(NH_3)_4(NO_3)_2$ as a noble-metal precursor and aluminum phosphate ($AlPO_4$) as a support in a $Pd(NH_3)_4(NO_3)_2$:phosphate mass ratio of 0.014:1 and subsequently calcining the mixture at 400 °C in air and reducing in a H_2/Ar atmosphere. According to a previous study, the NH_3 ligand in the aqueous $[Pd(NH_3)_4]^{2+}$ cation is easily substituted by the surface OH groups of the $AlPO_4$ support, and the strong interaction between $AlPO_4$ and $Pd(NH_3)_4(NO_3)_2$ contributes to the suppression of Pd sintering during the calcination and reduction processes [20]. The diffuse reflectance infrared Fourier-transform (DRIFT) spectrum of the dehydrated $AlPO_4$ support shows obvious and weak signals at 3655 and 3750 cm^{-1}, respectively, indicating that most $AlPO_4$ surface groups are P–OH rather than Al–OH (Fig. S1A) [21,22]. After Pd loading, the intensity of the P–OH peak drastically decreased, while the intensity of the Al–OH peak remained almost constant, indicating that P–OH groups were involved in the NH_3 ligand substitution and eventually generated a Pd–O–P interface. However, the amount of atomically dispersed Pd was low owing to the limited number of P–OH groups. Further increasing the $Pd(NH_3)_4(NO_3)_2$:phosphate mass ratio to 0.14:1 produced a composite catalyst containing both Pd single-atoms and nanoparticles ($Pd_{1+NP}/AlPO_4$). As a reference, a Pd nanoparticle-based catalyst ($Pd_{NP}/AlPO_4$) was fabricated by reducing $PdCl_2$ with $NaBH_4$ and

subsequently impregnating it with $AlPO_4$.

Powder X-ray diffraction (PXRD) peaks for these Pd-supported catalysts (i.e., $Pd_1/AlPO_4$, $Pd_{NP}/AlPO_4$, and $Pd_{1+NP}/AlPO_4$) matched well with those for standard tridymite-type $AlPO_4$, except for the appearance of Pd nanoparticle peak at 40.0° over the $Pd_{1+NP}/AlPO_4$ and $Pd_{NP}/AlPO_4$ catalysts (Fig. 1A). Inductively coupled plasma–optical emission spectroscopy (ICP–OES) revealed that $Pd_{1+NP}/AlPO_4$ and $Pd_{NP}/AlPO_4$ both contained similar Pd contents of 4.8–5.2 wt%, but $Pd_1/AlPO_4$ only contained 0.7 wt% Pd (Table S1). N_2 adsorption–desorption isotherms revealed that all the catalysts had an identical textural structure, with Brunauer–Emmett–Teller (BET) specific surface areas in the range 49.3–62.7 $m^2 \cdot g^{-1}$ (Table S1, Fig. S1B). Transmission electron microscopy (TEM) images revealed that $Pd_{1+NP}/AlPO_4$ and $Pd_{NP}/AlPO_4$ both had comparable Pd-nanoparticle sizes and distributions at 3.5 and 4.2 nm, respectively (Figs. S1C–F). X-ray energy-dispersive spectroscopy mappings indicated the uniform distribution of Pd, Al, P, and O atoms on the $Pd_{1+NP}/AlPO_4$ surface (Figs. S1G–K). High-angle annular dark-field scanning TEM (HAADF–STEM) images shown the excellent crystallinity of the $AlPO_4$ phase with a 200 crystal spacing of 0.250 nm and isolated atom-dispersed Pd atoms for both $Pd_{1+NP}/AlPO_4$ and $Pd_1/AlPO_4$ (Fig. 1C–D) [23]. In addition, some bended and ordered Pd nanoparticles with 111 crystal spacing of 0.220 nm were also detected on $Pd_{1+NP}/AlPO_4$ surface (Fig. 1 C and S2A–B) [24]. Fourier-transform infrared (FTIR) spectra of these $AlPO_4$-based catalysts show peaks at 1130, 720, and 485 cm^{-1}, which are assigned to P–O bending, Al–O stretching, and Al–O bending mode vibrations, respectively (Figs. S2C) [25]. During high-temperature calcination, the surface OH group was removed, as indicated by the weak OH characteristic peak (at approximately 3600 cm^{-1}). High-resolution X-ray photoelectron spectroscopy (XPS) revealed Pd $3d_{5/2}$ and $3d_{3/2}$ peaks (at 335.5 and 340.8 eV) for metallic Pd^0 in $Pd_{NP}/AlPO_4$ and Pd $3d_{5/2}$ and $3d_{3/2}$ peaks (at 337.8 and 343.0 eV) for oxidized Pd in $Pd_1/AlPO_4$, respectively, which indicates that the Pd^{2+}–O pair was generated over $Pd_1/AlPO_4$ [24,26]. Synthetically, XPS spectrum for the as-synthesized $Pd_{1+NP}/AlPO_4$ possesses both Pd^0 and Pd^{2+} signals, from which the Pd^{2+}/Pd^0 ratio was estimated at
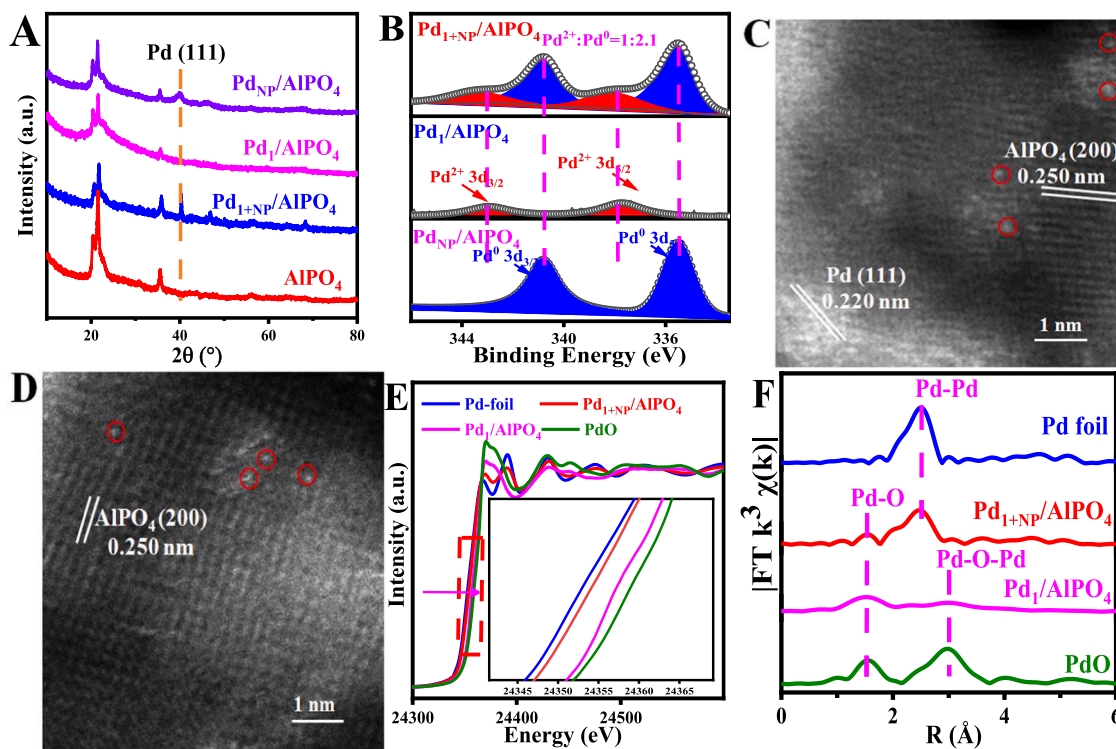
Fig. 1. (A) PXRD pattern, (B) Pd 3d XPS analysis of catalysts; HAADF-STEM image of (C) $Pd_{1+NP}/AlPO_4$ and (D) $Pd_1/AlPO_4$; (E) Pd XANES spectra and (F) FT-EXAFS analysis of $Pd_{1+NP}/AlPO_4$ and $Pd_1/AlPO_4$.

1:2.1. The Al and P 2*p* spectra show $2p_{3/2}$ and $2p_{1/2}$ peaks associated with oxidative Al^{3+} (at 74.3 and 74.9 eV, respectively) and P^{5+} states (at 133.5 and 134.3 eV), which are consistent with the valence state of the stoichiometric formula (Figs. S2D–E) [24,25,27,28]. Correspondingly, the O 1*s* spectrum exhibits an O^{2-} peak at 532.7 eV, which corresponds to PO_4^{3-}, including Al–O–P and Pd–O–P bonds (Fig. S2F) [25]. Pd K-edge X-ray absorption near-edge structure spectroscopy (XANES) was used to investigate the atomic coordination environment of Pd species. The Pd-coordination environment was analyzed using extended X-ray absorption fine-structure (EXAFS) spectroscopy. The Pd XANES spectra revealed that the X-ray absorption energy decreased in the order PdO > $Pd_1/AlPO_4$ > $Pd_{1+NP}/AlPO_4$ > Pd foil (Fig. 1E). Meanwhile, the Fourier-transform (FT) k^3-weighted $\chi(k)$ EXAFS (FT–EXAFS) spectrum for $Pd_1/AlPO_4$ revealed a noticeable peak attributed to the Pd–O structure at 1.6 Å, which confirmed that the predominant species was isolated Pd (Fig. 1 F) [29–32]. The spectrum for $Pd_{1+NP}/AlPO_4$ showed peaks corresponding to Pd–O and Pd–Pd coordinations at 1.6 and 2.4 Å, respectively, which agrees with the corresponding XRD pattern and HR-TEM image [30]. The results show that the $Pd_{1+NP}/AlPO_4$ catalyst is modeled based on $AlPO_4$ and supported by both Pd single atoms at the Pd–O–P interface and nanoparticles possessing a bare Pd surface.

3.2. Hydrogenolysis–hydrogenation of furan alcohols

First, the activity of the $Pd/AlPO_4$ catalysts was evaluated in the furan alcohol (FA) reaction in tetrahydrofuran at 30 °C and a H_2 pressure of 4.0 MPa. Because of the low reaction temperature, a high carbon balance of 99.0% could be obtained. As shown in the temporal evolution curve of the product distribution, $Pd_{NP}/AlPO_4$, $Pd_1/AlPO_4$ and $Pd_{1+NP}/AlPO_4$ exhibited completely different catalytic performance with identical Pd^0 or Pd^{2+} contents (Fig. 2A-2 C). $Pd_{NP}/AlPO_4$ showed catalytic C═C hydrogenation properties, including a 29.3% FA conversion rate and 100% selectivity for tetrahydrofuran alcohol (THFA) after 6 h. In contrast, $Pd_1/AlPO_4$ showed the opposite hydrogenolysis path for the C–OH bond and generated 2-methylfuran (MF) as the main product. Correspondingly, the THFA selectivity was below 10%. $Pd_{1+NP}/AlPO_4$ showed a tandem hydrogenolysis–hydrogenation route with a large amount of hydrogenolyzed MF and subsequently hydrogenated 2-methyltetrahydrofuran (THMF). To exclude a possible path for synthesizing THMF via FA hydrogenation and subsequent THFA hydrogenolysis, a controlled experiment was conducted using THFA as the starting material, which is inert at ambient temperatures (Fig. S3A). Additionally, previous reports have suggested that THFA is relatively inert and only activated for hydrogenolysis above 120 °C [33,34]. By prolonging the reaction to 12 h, the MF intermediate was completely converted, and the THMF yield reached 83.3% over $Pd_{1+NP}/AlPO_4$ (Fig. 2D, Table 1 entry 1). Compared with previously reported catalysts, including $IrIrO_x/C$, $PdCu/ZrO_2$, and Cu–Ni–Re/Hβ, the $AlPO_4$-based catalysts showed an unprecedented efficiency for producing THMF. Particularly, the reaction temperature substantially decreased from the previously reported range 220 °C–240 °C to 30 °C (Table S2) [14,15,17]. Moreover, compared with classical conditions previously reported for sole hydrogenolysis reactions, our reaction condition over $Pd_1/AlPO_4$ for synthesizing MF is also the greenest, not to mention the cascade hydrogenolysis–hydrogenation over $Pd_{1+NP}/AlPO_4$ for further MF upgrading (Table 1 entry 2, Table S2) [35–38]. Furthermore, after five cycles, the spent $Pd_{1+NP}/AlPO_4$ catalyst showed a stable activity without any apparent decay of either the FA conversion rate or THMF selectivity (Fig. S3B). PXRD, XPS, ICP–OES, and N_2 adsorption–desorption revealed the $Pd_{1+NP}/AlPO_4$ catalyst's stable crystal structure, Pd distribution, and valence states under these reaction conditions (Figs. S3C–H, Table S1). Similarly, the $Pd_1/AlPO_4$ catalyst was also robust and stably generated MF during cycling (Fig. S3I).

Subsequently, $Pd_{1+NP}/AlPO_4$-catalyzed tandem hydrogenolysis–hydrogenation was applied to a wide range of furan alcohols. 5-Methylfuran alcohol (MFA) is a typical biomass derivative, which is

easily formed via the selective C═O hydrogenation of 5-methylfurfural [5]. It can be converted to the corresponding tetrahydrofuran, 2,5-dimethyltetrahydrofuran (THDMF), through identical reaction pathways, supported by the time-dependent product distributions (Figs. S4A–C). The catalytic results still follow with identical trends: $Pd_{1+NP}/AlPO_4$ shows the selective synthesis of THDMF (73.1% selectivity), whereas $Pd_{NP}/AlPO_4$ and $Pd_1/AlPO_4$ show the selective synthesis of 5-methyltetrahydrofuran alcohol (THMFA) and 2,5-dimethylfuran (DMF), respectively (Fig. 2E, Table 1 entries 3–4). Similarly, 2,5-dihydroxymethyl furan, the C═O hydrogenated derivative of 5-hydroxymethylfurfural, also showed a high catalytic conversion rate of 100% and a corresponding selectivity of 66.2% for THDMF (Table 1 entry 5) [6]. To the best of our knowledge, our catalyst enabled the one-pot tandem synthesis of THDMF at an ambient temperature for the first time, while the catalytic activity still surpassed those previously reported for tandem syntheses over complex catalysts (such as Cu/MgAlO and Cu/ZnO–Al_2O_3) in the range 180 °C–220 °C (Table S3) [39,40]. As in the MFA reaction, the $Pd_1/AlPO_4$ catalyst only showed the hydrogenolysis route, affording a 81.9% selectivity of DMF (Table 1 entry 6). Meanwhile, other furan alcohols (such as 5-ethylfuran alcohol and 3-furan alcohol) and heterocyclic alcohols (such as 2-thiophene alcohol, 2-pyridine alcohol) showed identical hydrogenolysis–hydrogenation and hydrogenolysis performances over $Pd_{1+NP}/AlPO_4$ and $Pd_1/AlPO_4$, respectively (Table 1, entries 7–14). Notably, for 2-benzofuran alcohol, 2-methylbenzofuran cannot be hydrogenated because of the stronger conjugated C═C structure (Table 1 entries 15–16). In addition, we demonstrated the oriented synthesis of 2-ethyltetrahydrofuran and 2-ethylfuran from furan methyl alcohol (Table 1 entries 17–18), which indicates the excellent universality of the proposed synthesis route comprising the initial C–OH hydrogenolysis and subsequent C═C hydrogenation.

3.3. Hydrogenation–hydrogenolysis–hydrogenation of furfurals

Compared with furan alcohols (e.g., FA, MFA, and 2,5-dihydroxymethylfuran), methyltetrahydrofurans synthesized from furan aldehydes (e.g., furfural, 5-methylfurfural, and 5-hydroxymethylfurfural) via one-pot hydrogenation–hydrogenolysis (i.e., sequential furfural C═O hydrogenation and FA hydrogenolysis steps) are scientifically and practically more important owing to the higher renewable priority of feedstocks. Gratifyingly, the $Pd_{1+NP}/AlPO_4$ catalyst also had a considerable C═O hydrogenation ability at an ambient temperature and exhibited a 100% furfural conversion rate and 71.6% THMF selectivity (Fig. 2F, S5A, Table S4) [12,14–17,41,42]. Meanwhile, the product evolutions for both 5-methylfurfural and 5-hydroxymethylfurfural were highly similar to those for the furfural reaction under the unprecedentedly mild reaction condition for THDMF synthesis (Fig. 2G–H and S5B–C, Table S4) [39,40,43–46]. Undoubtedly, these are the mildest reaction conditions ever reported for synthesizing THMF and THDMF to date.

3.4. Identification of hydrogenolysis and hydrogenation sites

According to the change in the concentrations of the MF-based products (MF and THMF) or THFA over time, C═C hydrogenation and C–OH hydrogenolysis were both pseudo-first-order reactions over $Pd_{1+NP}/AlPO_4$, $Pd_1/AlPO_4$, and $Pd_{NP}/AlPO_4$ (Fig. 3A–B). Furthermore, the relationship between the initial generation rate of MF-based products or THFA concerning different FA concentrations shows that the hydrogenolysis and hydrogenation reaction orders were in the range 0.91–0.98 for FA (Fig. 3 C, S6A–D). Correspondingly, these reaction rates are slightly related to H_2 pressures in the range 1.0–5.0 MPa and a virtually zero reaction order (in the range 0.01–0.09) for H_2 (Figs. S6E–I), which is widely observed for noble-metal-catalyzed hydrogenolysis/hydrogenation reactions and is expected if the FA rather than H_2 activation rate determines the hydrogenation step [25, 26,47–49]. At 30 °C, the FA hydrogenolysis rates decreased in the order
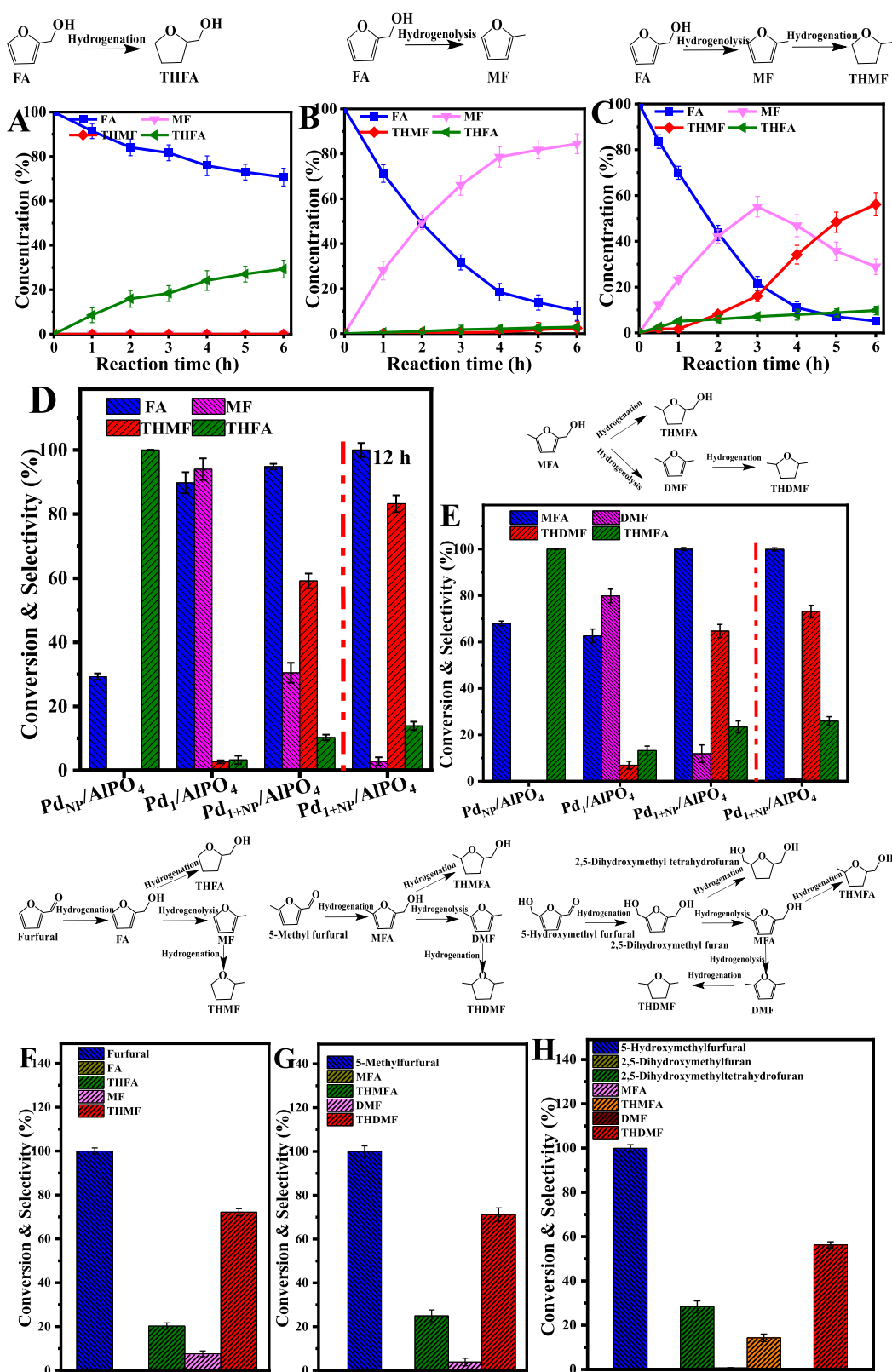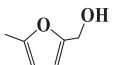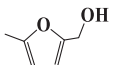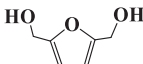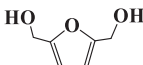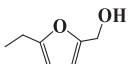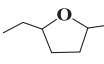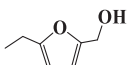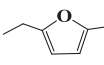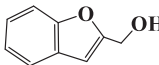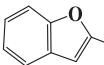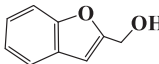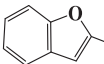
Fig. 2. Reaction pathway and time-dependent product concentration and reaction pathway of FA reaction over (A) Pd$_{NP}$/AlPO$_4$, (B) Pd$_1$/AlPO$_4$ and (C) Pd$_{1+NP}$/AlPO$_4$; (D) Catalytic performance of FA reaction over various catalysts; (E) Reaction pathway and catalytic performance of MFA reaction over various catalysts; Reaction pathway and catalytic performance of Pd$_{1+NP}$/AlPO$_4$ in (F) furfural, (G) 5-methylfurfural, (H) 5-hydroxymethyl furfural reaction. Reaction conditions: tetrahydrofuran (10 mL), Pd$_{1+NP}$/AlPO$_4$ (0.05 g) or Pd$_{NP}$/AlPO$_4$ (0.035 g) or Pd$_1$/AlPO$_4$ (0.115 g), temperature 30 °C, 4.0 MPa H$_2$. (A-C) FA (0.1 mmol), (D,E) FA (0.1 mmol), time 6 h, (F) furfural (0.1 mmol), time 12 h; (G) 5-methyl furfural (0.1 mmol), time 12 h; (H) 5-hydroxymethyl furfural (0.1 mmol), time 12 h. The products were quantified by GC.

Table 1

The substrate scope of furan alcohols. Reaction conditions: $Pd_{1+NP}/AlPO_4$ (0.05 g) or $Pd_1/AlPO_4$ (0.115 g), reactant (0.1 mmol), tetrahydrofuran (10 mL), temperature 30 °C, 4.0 MPa H_2. The products were quantified by GC.

Entry	Reactant	Catalyst	Time (h)	Product	Conversion (%)	Selectivity (%)
1		$Pd_{1+NP}/AlPO_4$	12		100	83.3
2		$Pd_1/AlPO_4$	6		89.8	94.1
3		$Pd_{1+NP}/AlPO_4$	12		100	73.1
4		$Pd_1/AlPO_4$	6		62.7	79.9
5		$Pd_{1+NP}/AlPO_4$	12		100	66.2
6		$Pd_1/AlPO_4$	6		73.4	81.9
7		$Pd_{1+NP}/AlPO_4$	12		100	68.9
8		$Pd_1/AlPO_4$	6		66.8	73.9
9		$Pd_{1+NP}/AlPO_4$	12		100	76.5
10		$Pd_1/AlPO_4$	6		84.8	71.1
11		$Pd_{1+NP}/AlPO_4$	12		100	86.5
12		$Pd_1/AlPO_4$	6		83.5	91.4
13		$Pd_{1+NP}/AlPO_4$	12		96.3.	52.5
14		$Pd_1/AlPO_4$	6		73.4	71.2
15		$Pd_{1+NP}/AlPO_4$	12		95.7	94.6
16		$Pd_1/AlPO_4$	6		78.5	91.2
17		$Pd_{1+NP}/AlPO_4$	12		100	56.3
18		$Pd_1/AlPO_4$	6		86.3	75.5
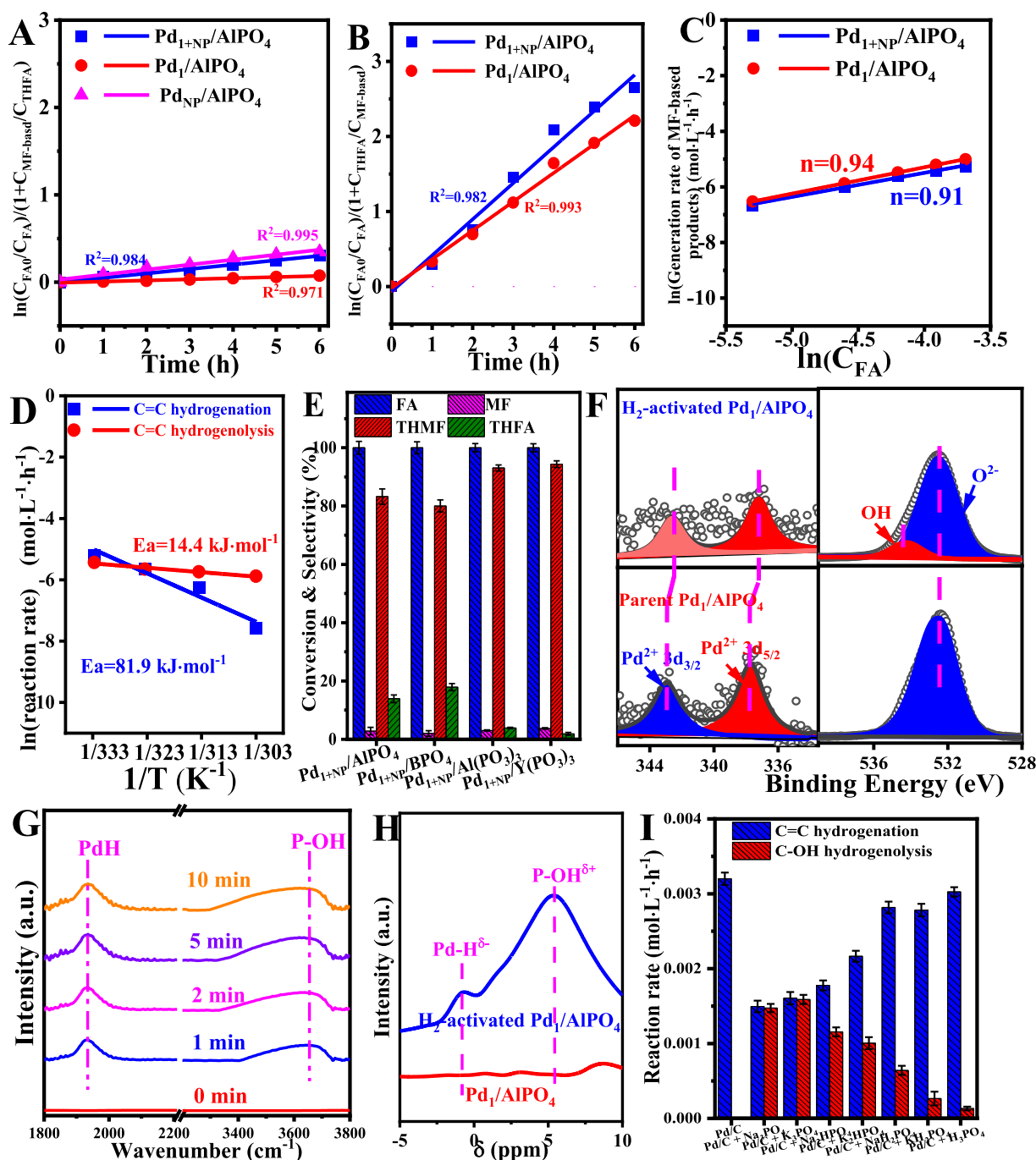
Fig. 3. (A) C=C hydrogenation and (B) C–OH hydrogenolysis kinetic over different catalysts; (C) C–OH hydrogenation kinetic experiments over different catalysts under different FA concentrations. (D) C=C hydrogenation and C–OH hydrogenolysis activation energy over $Pd_{1+NP}/AlPO_4$; (E) Catalytic performance of FA reaction over various catalysts; (F) Pd and O speciation of H_2-activated $Pd_1/AlPO_4$ followed by the in situ NAP-XPS at 30 °C; (G) In situ IR spectra for H_2-activated $Pd_1/AlPO_4$ at 30 °C; (H) Solid-state ^1H NMR for H_2-activated $Pd_1/AlPO_4$; (I) Catalytic performance of MFA reaction over Pd/C and various liquid PO_4^{3-}-containing compounds. Reaction conditions: $Pd_{1+NP}/AlPO_4$ (0.05 g) or $Pd_{NP}/AlPO_4$ (0.035 g) or $Pd_1/AlPO_4$ (0.115 g), tetrahydrofuran (10 mL), temperature 30 °C, 4.0 MPa H_2, FA (0.1 mmol), (C) FA (0.05, 0.1, 0.15, 0.2, 0.25 mmol), time 1 h, (D) FA (0.1 mmol), 0.5 h, (E) time 12 h, (I) Pd/C (0.05 g), PO_4^{3-}-containing compounds (0.1 mmol), time 1 h. The products were quantified by GC.

$Pd_1/AlPO_4$ (0.0028 mol·L^{-1}·h^{-1}) > $Pd_{1+NP}/AlPO_4$ (0.0025 mol·L^{-1}·h^{-1}) >> $Pd_{NP}/AlPO_4$ (0.0001 mol·L^{-1}·h^{-1}), whereas the corresponding FA hydrogenation rates decreased in the opposite order: $Pd_{NP}/AlPO_4$ (0.0009 mol·L^{-1}·h^{-1}) >> $Pd_{1+NP}/AlPO_4$ (0.0005 mol·L^{-1}·h^{-1}) > $Pd_1/AlPO_4$ (0.0001 mol·L^{-1}·h^{-1}) (Fig. S7A). With increasing reaction temperature in the range 30 °C–60 °C, the hydrogenolysis and hydrogenation rates both increased over $Pd_{1+NP}/AlPO_4$, whereas the selectivities of the hydrogenolyzed products (e.g., MF and THMF) were

reduced (Fig. S7B). The apparent activation energies of the C=O hydrogenation and C–OH hydrogenolysis were determined at 81.9 and 14.4 kJ·mol^{-1}, respectively, based on the Arrhenius equation (Fig. 3D). Owing to the physicochemical differences of these catalysts, we reasonably inferred that the hydrogenolysis and hydrogenation sites were mainly derived from the Pd–O–P interface and Pd nanoparticles, respectively. The $Pd_{1+NP}/AlPO_4$ catalyst showed a much higher reaction rate and lower activation energy for synthesizing MF compared to

THFA. This can explain why $Pd_{1+NP}/AlPO_4$, which contains both Pd–O–P interfaces and Pd nanoparticles, predominantly catalyzed C–OH hydrogenolysis instead of the parallel C═C hydrogenation.

To determine the role of the Pd–O–P interfaces, we synthesized a series of phosphate-supported Pd catalysts (i.e., Pd_{1+NP}/BPO_4, $Pd_{1+NP}/Al(PO_3)_3$, and $Pd_{1+NP}/Y(PO_3)_3$) by following the same method as that used to prepare $Pd_{1+NP}/AlPO_4$, which also showed a powerful catalytic hydrogenolysis–hydrogenation ability (Fig. 3E). Near-ambient-pressure XPS (NAP–XPS) was conducted *in situ* to investigate the changes in the surface chemical valence of $Pd_1/AlPO_4$. At 30 °C, after H_2 was added, the electron densities of the Al^{3+} and P^{5+} species were stable within the experimental detection limit of 0.1 eV (Figs. S7C–D). Differently, the Pd $3d_{5/2}$ and $3d_{3/2}$ peaks slightly shifted from 337.8 and 343.0 eV to lower binding energies at 337.2 and 342.3 eV, respectively (Fig. 3 F) [50]. Correspondingly, in the O 1 s spectrum, a peak corresponding to the P–OH bond appeared at 534.1 eV (Fig. 3F) [25,51]. This result indicates that H_2 could be activated at the Pd–O–P structure, and the H atom migrated from Pd to O sites and lost electrons to yield electron-withdrawing H^+ ($–OH^+$), whereas the other H atom at the Pd^{2+} site formed a partially negatively charged H^- species ($Pd–H^-$). Compared with the parent Pd–O–P, the charge-transformation-genera ted $Pd(H^-).(OH^+)P$ species possessed higher and lower electron densities for O and Pd, respectively. The H_2 heterolysis mechanism of $Pd_1/AlPO_4$ and $Pd_{1+NP}/AlPO_4$ was further verified via kinetic isotope experiments. The results showed that the hydrogenolysis rate was 3.01–3.20 times lower in D_2 than in H_2 (Fig. S7E,F) [52]. In contrast, hydrogenation over $Pd_{NP}/AlPO_4$ via the H_2 homolysis mechanism was only 1.81-times slower in D_2 than in H_2 (Fig. S7G). In addition, the ambient-temperature H_2 heterolysis was further investigated using in situ attenuated total reflectance infrared spectroscopy (ATR–IR). Over $Pd_1/AlPO_4$ and $Pd_{1+NP}/AlPO_4$, after H_2 was activated, the spectrum showed obvious peaks attributed to Pd–H and P–OH at 1927 and 3631 cm^{-1}, respectively (Fig. 3 G, S7H) [53,54]. However, $Pd_{NP}/AlPO_4$ cannot show the appearance of Pd–H and P–OH peaks, which may be ascribed to the instability of the active H atoms (Fig. S7H) [24]. Meanwhile, the coordination environment of the P species was recorded using solid-state ^{31}P magic-angle spinning nuclear magnetic resonance (MAS NMR) spectroscopy. The spectrum for the parent $Pd_1/AlPO_4$ exhibited only one peak at −30.1 ppm, which was assigned to either P–$(OAl)_4$ or P–$(OPd)(OAl)_3$ (Fig. S8A). After H_2 was activated, another peak appeared at −21.5 ppm and was assigned to P–$(OH)(OAl)_3$, and the signal at −30.1 ppm was attenuated [23,55]. In addition, the ^1H MAS NMR spectrum for H_2-activated $Pd_1/AlPO_4$ was sensitive to the ^1H coordination environment and exhibited two peaks at −0.8 and +5.3 ppm, which were attributed to the hydridic $Pd–H^-$ and P–OH species, respectively (Fig. 3H) [25,56]. These results clearly indicate that an intimate $H^+–H^-$ pair was generated in situ via the H_2-activated transformation from Pd–O–P to $Pd(H^-).(OH^+)P$.

To verify the role of PO_4^{3-} species in the catalytic reaction, the mixture of Pd/C and various liquid PO_4^{3-}-containing compounds were used as the catalyst for the MFA reaction. Pd/C showed a C═C hydrogenation ability without the generation of C–OH hydrogenolyzed products (DMF and THDMF) (Fig. 3F, S8B). The addition of Na_3PO_4/K_3PO_4 and Pd/C showed considerably bifunctional catalytic performance, including MFA conversion and hydrogenolyzed product (Figs. S8C–D). To our surprise, the addition of H_3PO_4 merely led to a decrease in C═C hydrogenation rate without affecting the intrinsic selectivity of Pd/C (Fig. S8E). More precisely, Na_2HPO_4/K_2HPO_4 and NaH_2PO_4/KH_2PO_4 possess middle hydrogenolysis activities, and hydrogenolysis rate followed the order of Na_3PO_4/K_3PO_4 (0.0014–0.0016 $mol·L^{-1}·g^{-1}·h^{-1}$) > Na_2HPO_4/K_2HPO_4 (0.0010–0.0011 $mol·L^{-1}·g^{-1}·h^{-1}$) > NaH_2PO_4/KH_2PO_4 (0.0002–0.0006 $mol·L^{-1}·g^{-1}·h^{-1}$) > H_3PO_4 (0.0001 $mol·L^{-1}·g^{-1}·h^{-1}$) (Fig. 3I, S8B–I). Generally, in the mainstream cognition, a stronger acidity is more conductive to bifunctional catalytic conversion by facilitating C–OH activation [57,58]. Whereas, we show a completely opposite finding, that is, a weaker acidic and a stronger alkaline catalytic system with

more free PO_4^{3-} anions can act as an acceptor of proton hydrogen, and the in situ generated $H^+–H^-$ pair in close proximity on the Pd–O–P interface largely promotes the hydrogenolysis process.

As mentioned above, the hydrogenolysis step requires efficient acidic sites for activating the C–OH bond. In agreed with previous reports, $Pd_1/AlPO_4$, $Pd_{NP}/AlPO_4$ and $Pd_{1+NP}/AlPO_4$ possess a pure Lewis acidity, as indicated by the single adsorbed peak of 1453 cm^{-1} observed in in situ pyridine-absorbed FTIR (Py-FTIR) spectra detected at 150 °C, which can be ascribed to the surface-uncoordinated Al^{3+} cations of the $AlPO_4$ support (Fig. 4A) [21,22,25]. Meanwhile, the temperature-programmed desorption of ammonia (NH_3-TPD) thermogram showed desorption peaks at 150 °C, which indicates weakly acidic Al^{3+} cations on the $AlPO_4$ surface (Fig. 4B). The Lewis-acid densities of the parent $Pd_1/AlPO_4$ and $Pd_{NP}/AlPO_4$ were both in the range 0.115–0.125 $mmol·g^{-1}$ (Table S5) [59]. However, at 300 °C, the Lewis-acid density substantially decreased to the range 0.035–0.047 $mmol·g^{-1}$ (Fig. S9A, Table S5). After H_2 activation, the Py–FTIR spectrum exhibited a peak at 1542 cm^{-1} over $Pd_1/AlPO_4$, which was attributed to a Brønsted acid. The Brønsted-acid density calculated using the Emeis equation only negligibly decreased from 0.049 to 0.040 $mmol·g^{-1}$ (at 150 °C and 300 °C, respectively), and the corresponding Brønsted/Lewis-acid molar ratio increased from 0.45 to 0.93. Correspondingly, the NH_3–TPD thermogram showed a markedly stronger peak for acid desorption in the range 350 °C–450 °C. Similar to $Pd_1/AlPO_4$, $Pd_{1+NP}/AlPO_4$ with abundant single Pd atoms also shows the transformation of Lewis acidity to Brønsted acidity (Fig. 4B, Table S5). In contrast, H_2-activated $Pd_{NP}/AlPO_4$ showed almost the same acidity as the parent counterpart. This confirms the strong Brønsted acidity of $Pd(H^-).(OH^+)P$, which ultimately promotes the selective activation of C–OH moieties.

The molecular interaction between the FA and catalyst surface was investigated using ATR–IR spectroscopy (Fig. 4C). Over $Pd_{NP}/AlPO_4$, the peak attributed to unsaturated C═C bonds redshifted from 1025 to 965 cm^{-1}, while the peak attributed to the saturated C–OH moiety did not move. This suggests that FA was chemisorbed on the surface of the Pd nanoparticles via the selective activation of the furan ring, which was oriented in a flat adsorption configuration [23,25,26]. Over parent $Pd_1/AlPO_4$, the signals for both the furan and C–OH moieties were weak probably because FA weakly chemisorbed on the surface of the $Pd_1/AlPO_4$ parent. After H_2 was activated, $Pd_{NP}/AlPO_4$ still showed a flat adsorption configuration, which agreed with the catalytic hydrogenation route. However, the spectrum for H_2-activated $Pd_1/AlPO_4$ showed a distinct FA signal and a redshifted C–OH peak while the C═C peak did not change, which suggests that H_2-activated $Pd_1/AlPO_4$ was oriented in a vertical adsorption configuration [60,61]. The strongly Brønsted acidic H^+ predominantly attached to the C–OH moiety via hydrogen-bond interactions and simultaneously hindered the furan-ring moiety from approaching the metal surface. These results indicate that the generation of the $Pd(H^-).(OH^+)P$ pair was the preliminary step for the tandem C–OH dehydration and hydrogenation at PO–H^+ and Pd–H^- sites, respectively, which controlled the selective C–OH hydrogenolysis route. Following the same reason, because the asymmetric C═O bond could be selectively hydrogenated, the C═O hydrogenation of furan aldehydes was further integrated in the proposed one-pot method for synthesizing methyltetrahydrofurans.

To further distinguish the adsorption capacities of the furan moiety and C–OH bond, an adsorption experiment of FA and MF was conducted (Figs. S9B–I). Compared with the $Pd_1/AlPO_4$ parent, $Pd_{NP}/AlPO_4$ adsorbed much more FA and MF (both 45.6% vs. 4.0%, 45.2% vs. 10.5%, respectively), which indicates that the Pd surface is beneficial for adsorbing the furan moiety (Fig. 4D,E). The H_2-activated $Pd_{NP}/AlPO_4$ showed similar adsorptions with $Pd_{NP}/AlPO_4$ parent, whereas the H_2-activated $Pd_1/AlPO_4$ adsorbed less MF (6.3% vs. 10.5%) but more FA (62.6% vs. 4.0%) than the $Pd_1/AlPO_4$ parent, which further suggests that the C–OH moiety adsorbed at the $H^+–H^-$ site. In addition, furan rings adsorbed on Pd-nanoparticle surfaces, which could explain the
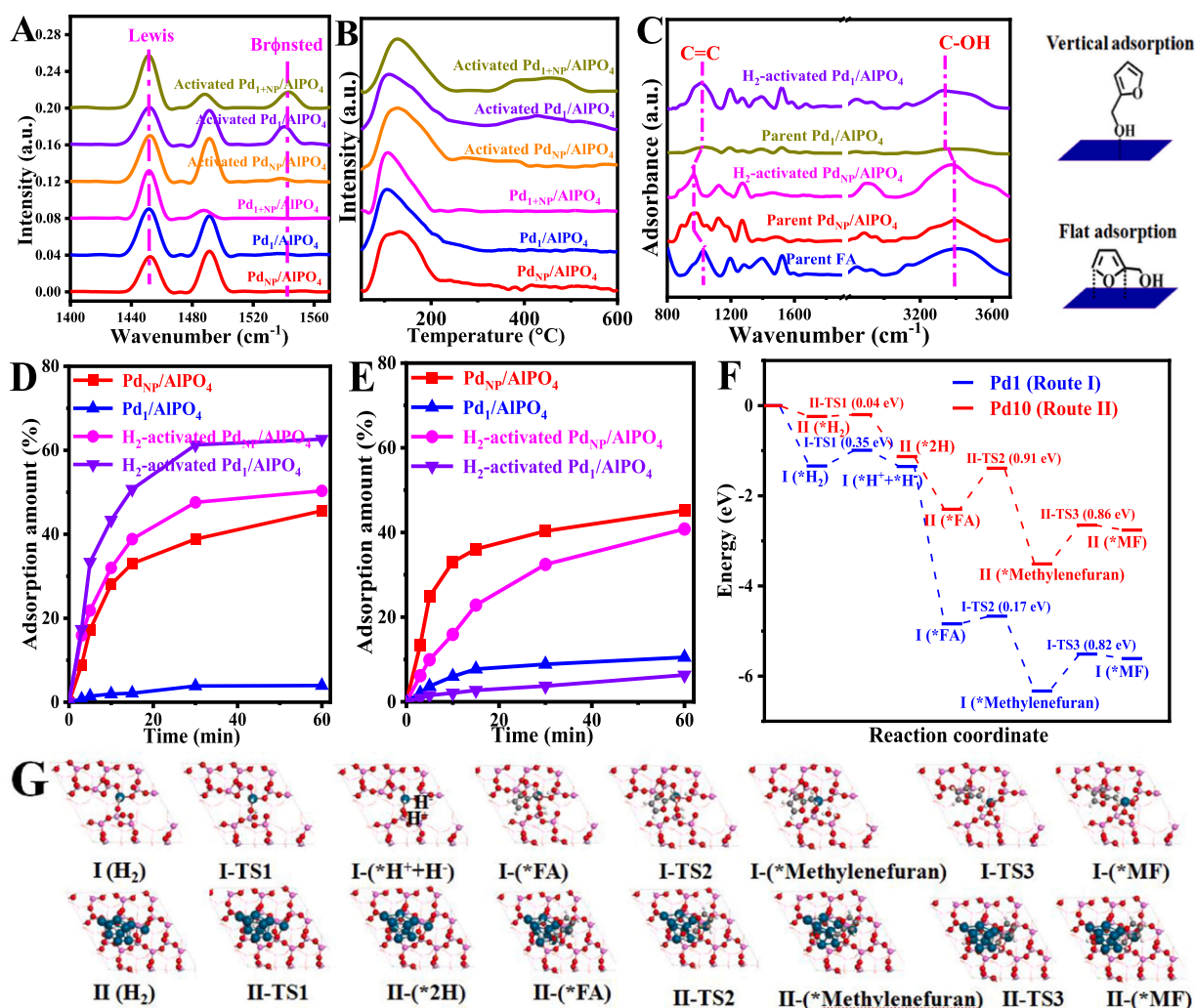
Fig. 4. (A) Py-FTIR spectra (detected at 150 °C) and (B) NH₃-TPD profiles of Pd₁/AlPO₄, Pd_NP/AlPO₄, Pd_{1+NP}/AlPO₄ and H₂-activated Pd₁/AlPO₄, Pd_NP/AlPO₄ and Pd_{1+NP}/AlPO₄; (C) ATR-IR spectra of adsorbed FA on various catalysts. The adsorption kinetics of (D) FA and (E) MF over different catalysts. Adsorption conditions: tetrahydrofuran (10 mL), Pd_{1+NP}/AlPO₄ (0.05 g) or Pd₁/AlPO₄ (0.05 g), FA (0.01 mmol) or MF (0.01 mmol), temperature 30 °C. The FA concentrations were quantified by Ultraviolet–Visible Spectroscopy. (F) Energy profile and (G) corresponding structural models for the catalytic hydrogenation and hydrogenolysis of FA.

high C=C hydrogenation activities of FA and MF over the Pd_NP/AlPO₄ and Pd_{1+NP}/AlPO₄ catalysts. The efficient synergy between Pd single-atom sites and nanoparticles in the Pd_{1+NP}/AlPO₄ catalyst ensures an unprecedented THMF formation efficiency under mild reaction conditions.

To further understand the catalytic mechanism of Pd single-atom and nanoparticle, density functional theory calculations were performed using a single Pd atom deposited AlPO₄ and a Pd cluster of 10 Pd atoms deposited AlPO₄ as simple models to represent the Pd₁/AlPO₄ and Pd_NP/AlPO₄ (Figs. S10A–B). H₂ is easily adsorbed on the Pd₁/AlPO₄ and Pd_NP/AlPO₄ with adsorption energies of –1.34 eV and –0.24 eV, respectively. Over Pd₁/AlPO₄, *H₂ undergoes heterolytic decomposition with an activation energy of 0.35 eV and exothermicity by –0.01 eV (Fig. 4 F,G), and Pd(H⁻).(OH⁺)P structure is formed in which one H is adsorbed on the Pd site to form H⁻ and the other H can be stabilized by the O site. Differently, *H₂ undergoes homolytic decomposition over Pd_NP/AlPO₄ with an activation energy of 0.04 eV and exothermicity by –0.89 eV, and two H are adsorbed on the Pd surface. For the adsorption of FA, calculations indicate that the adsorption energy of vertical adsorption mode on the Pd₁/AlPO₄ (–2.62 eV) is higher than that of flat-lying adsorption mode (–1.93 eV) (Fig. S10C–D). Whereas, FA is preferentially horizontally adsorbed on the Pd_NP/AlPO₄ with a higher adsorption energy (–2.73 vs –1.07 eV) (Figs. S10E–F). After the H₂ activation, the

presence of Pd(H⁻).(OH⁺)P results in a strong adsorption (–3.48 eV) of the C–OH group in FA through intermolecular hydrogen bond interactions (Fig. S10G–J), which is highly consistent with the above-mentioned adsorption and ATR-IR results. Selective activation and protonation of the C–OH group can remove H₂O with an energy barrier of 0.17 eV and exothermicity of –1.49 eV. Subsequently, the other H combines with the methylene group to produce MF with energy barrier of 0.82 eV and endothermicity of 0.72 eV. Whereas, for the C=C hydrogenation route on Pd_NP/AlPO₄, the energy barrier for the combination of Pd-H with C=C group is as high as 0.91 eV. Combining the weaker adsorption energy of furan on Pd₁₀, these results can be used to explain the preferential hydrogenolysis of C–OH group rather than hydrogenation of C=C over Pd_{1+NP}/AlPO₄. Considering the rapid H₂ dissolution rate and rate-determining step of the methylene hydrogenation, the theoretical rate possesses reaction order of 0 for H₂ pressure and 1 for FA, which are very close to the experimentally measured values of 0.02 and 0.90 (Table S6). Therefore, the presence of Pd₁-(OP)₄ on Pd_{1+NP}/AlPO₄ facilitates H₂ heterolysis, and the in situ–generated H⁺–H⁻ pair is conducive to the selective hydrogenolysis of -OH moiety of FA.

4. Conclusions

Pd supported phosphates containing abundant Pd–O–P interfaces and bare Pd-nanoparticle surfaces could accelerate the hydrogenolysis–hydrogenation of furan alcohols into methyltetrahydrofurans at ambient temperatures. The highly efficient synergistic catalysis arises from the H^-–Pd.(OH^+)P pair generated in situ via H_2 heterolysis, which simultaneously provided acidic and hydrogenation sites for C–OH dehydration and hydrogenation for the hydrogenolysis process. Additionally, the surface of the bare Pd nanoparticles could promote the hydrogenation of in situ generated methylfurans. Furthermore, C=O hydrogenation and hydrogenolysis–hydrogenation were both integrated in the one-pot synthesis of methyltetrahydrofurans from furan aldehydes. This study provides a powerful strategy for using simple phosphate-supported catalysts for synthesizing biobased high-value biofuels and chemicals.

CRediT authorship contribution statement

Zou Ji-Jun: Investigation. **Deng Qiang:** Project administration, Supervision, Writing – original draft. **Lu Jialuo:** Methodology, Writing – original draft. **Liu Yong:** Data curation, Software. **Wang Jun:** Conceptualization. **Zeng Zheling:** Investigation. **Chen Lungang:** Investigation. **Deng Shuguang:** Resources.

Declaration of Competing Interest

The authors declare not competing financial interest.

Data Availability

Data will be made available on request.

Acknowledgements

Supporting Information

Supplemental Information includes experimental procedures, Figs. S1-S10 and Tables S1-S6.

Appendix A. Supporting information

Supplementary data associated with this article can be found in the online version at doi:10.1016/j.apcatb.2023.123622.

References

[1] G.W. Huber, J.N. Chheda, C.J. Barrett, J.A. Dumesic, Production of liquid alkanes by aqueous-phase processing of biomass-derived carbohydrates, Science 308 (2005) 1446–1450.

[2] H. Zhao, J.E. Holladay, H. Brown, Z.C. Zhang, Metal chlorides in ionic liquid solvents convert sugars to 5-hydroxymethylfurfural, Science 316 (2007) 1597–1600.

[3] Y. Román-Leshkow, J.N. Chheda, J.A. Dumesic, Phase modifiers promote efficient production of hydroxymethylfurfural from fructose, Science 312 (2006) 1933–1937.

[4] R. Mariscal, P. Maireles-Torres, M. Ojeda, I. Sádaba, M.L. Granados, Furfural: a renewable and versatile platform molecule for the synthesis of chemicals and fuels, Energy Environ. Sci. 9 (2016) 1144–1189.

[5] Y. Román-Leshkow, C.J. Barrett, Z.Y. Liu, J.A. Dumesic, Production of dimethylfuran for liquid fuels from biomass-derived carbohydrates, Nature 447 (2007) 982–985.

[6] J. Fu, J. Lym, W. Zheng, K. Alexopoulos, A.V. Mironenko, N. Li, J.A. Boscoboinik, D. Su, R.T. Weber, D.G. Vlachos, C–O bond activation using ultralow loading of noble metal catalysts on moderately reducible oxides, Nat. Catal. 3 (2020) 446–453.

[7] K.A. Goulas, A.V. Mironenko, G.R. Jenness, T. Mazal, D.G. Vlachos, Fundamentals of C–O bond activation on metal oxide catalysts, Nat. Catal. 2 (2019) 269–276.

[8] J. Zhang, L.D. Ellis, B. Wang, M.J. Dzara, C. Sievers, S. Pylypenko, E. Nikolla, J.W. Medlin, Control of interfacial acid–metal catalysis with organic monolayers, Nat. Catal. 1 (2018) 148–155.

[9] E. Latifi, A.D. Marchese, M.C.W. Hulls, D.V. Soldatov, M. Schlaf, [Ru(triphos)(CH$_3$CN)$_3$](OTf)$_2$ as a homogeneous catalyst for the hydrogenation of biomass derived 2,5-hexanedione and 2,5-dimethyl-furan in aqueous acidic medium, Green. Chem. 19 (2017) 4666–4679.

[10] Y.L. Louie, J. Tang, A.M.L. Hell, A.T. Bell, Kinetics of hydrogenation and hydrogenolysis of 2,5-dimethylfuran over noble metals catalysts under mild conditions, Appl. Catal. B 202 (2017) 557–568.

[11] J.G. Stevens, R.A. Bourne, M.V. Twigg, M. Poliakoff, Real-time product switching using a twin catalyst system for the hydrogenation of furfural in supercritical CO$_2$, Angew. Chem. Int. Ed. 49 (2010) 8856–8859.

[12] P. Liu, L. Sun, X. Jia, C. Zhang, W. Zhang, Y. Song, H. Wang, C. Li, Efficient one-pot conversion of furfural into 2-methyltetrahydrofuran using non-precious metal catalysts, Mol. Catal 490 (2020), 110951.

[13] F. Dong, Y. Zhu, G. Ding, J. Cui, X. Li, Y. Li, One-step conversion of furfural into 2-methyltetrahydrofuran under mild conditions, ChemSusChem 8 (2015) 1534–1537.

[14] Y. Peng, Z. Xu, L. Yu, X. Li, W. Yang, Trimetallic Cu-Ni-Re/Hβ catalyst for the direct conversion of furfural to 2-methyltetrahydrofuran, Chem. Eng. J. 454 (2023), 139746.

[15] X. Chang, A.F. Liu, B. Cai, J.Y. Luo, H. Pan, Y.B. Huang, Catalytic transfer hydrogenation of furfural to 2-methylfuran and 2-methyltetrahydrofuran over bimetallic copper-palladium catalysts, ChemSusChem 9 (2016) 3330–3337.

[16] B. Seemala, C.M. Cai, R. Kumar, C.E. Wyman, P. Christopher, Effects of Cu-Ni bimetallic catalyst composition and support on activity, selectivity, and stability for furfural conversion to 2-methylfuran, ACS Sus. Chem. Eng. 6 (2018) 2152–2161.

[17] N.S. Date, A.M. Hengne, K.-W. Huang, R.C. Chikate, C.V. Rode, Single pot selective hydrogenation of furfural to 2-methylfuran over carbon supported iridium catalysts, Green. Chem. 20 (2018) 2027–2037.

[18] S. Liu, P.A. Kots, B. Vance, A. Danielson, D.G. Vlachos, Plastic waste to fuels by hydrocracking at mild conditions, Sci. Adv. 7 (2021), eabf8283.

[19] D. Wu, W.Y. Hernández, S. Zhang, E.I. Vovk, X. Zhou, Y. Yang, A.Y. Khodakov, V.V. Ordomsky, In situ generation of Brønsted acidity in the Pd-I bifunctional catalysts for selective reductive etherification of carbonyl compounds under mild conditions, ACS Catal. 9 (2019) 2940–2948.

[20] X. Li, H. Su, D. Li, H. Chen, X. Yang, S. Wang, Highly dispersed Pd/AlPO-5 catalyst for catalytic hydrogenation of 2-ethylanthraquinone, Appl. Catal. A 528 (2016) 168–174.

[21] J.M. Campelo, M. Jaraba, D. Luna, R. Luque, J.M. Marinas, A.A. Romero, Effect of phosphate precursor and organic additives on the structural and catalytic properties of amorphous mesoporous AlPO$_4$ materials, Chem. Mater. 15 (2003) 3352–3364.

[22] M. Machida, S. Minami, K. Ikeue, S. Hinokuma, Y. Nagao, T. Sato, Y. Nakahara, Rhodium nanoparticle anchoring on AlPO$_4$ for efficient catalyst sintering suppression, Chem. Mater. 26 (2014) 5799–5805.

[23] F. Gutiérrez-Mora, K.C. Goretta, D. Singh, J.L. Routbort, S. Sambasivan, K.A. Steiner, J. Adabie, K.K. Rangan, High-temperature deformation of amorphous AlPO$_4$-based nano-composites, J. Eur. Ceram. Soc. 26 (2006) 1179–1183.

[24] Q. Deng, R. Zhou, Y.-C. Zhang, X. Li, J. Li, S. Tu, G. Sheng, J. Wang, Z. Zeng, T. Yoskamtorn, S.C.E. Tsang, H$^+$-H$^-$ pairs in partially oxidized MAX phases for bifunctional catalytic conversion of furfurals into linear ketones, Angew. Chem. Int. Ed. 62 (2023), e202211461.

[25] W. Fang, A. Riisager, Efficient valorization of biomass-derived furfural to fuel bio-additive over aluminum phosphate, Appl. Catal. B 298 (2021), 120575.

[26] Q. Deng, X. Hou, Y. Zhong, J. Zhu, J. Wang, J. Cai, Z. Zeng, J.-J. Zou, S. Deng, T. Yoskamtorn, S.C.E. Tsang, 2D MOF with compact catalytic sites for the one-pot synthesis of 2,5-dimethylfuran from saccharides via tandem catalysis, Angew. Chem. Int. Ed. 61 (2022), e202205453.

[27] T. Mitsudome, M. Sheng, A. Nakata, J. Yamasaki, T. Mizugaki, K. Jitsukawa, Cobalt phosphide catalyst for hydrogenation of nitriles, Chem. Sci. 11 (2020) 6682–6689.

[28] X. Jin, R. Tsukimura, T. Aihara, H. Miura, T. Shishido, K. Nozaki, Metal–support cooperation in Al(PO$_3$)$_3$-supported platinum nanoparticles for the selective hydrogenolysis of phenols to arenes, Nat. Catal. 4 (2021) 312–321.

[29] Y. Zhao, H. Zhou, W. Chen, Y. Tong, C. Zhao, Y. Lin, Z. Jiang, Q. Zhang, Z. Xue, W.-C. Cheong, B. Jin, F. Zhou, W. Wang, M. Chen, X. Hong, J. Dong, S. Wei, Y. Li, Y. Wu, Two-step carbothermal welding to access atomically dispersed Pd$_1$ on three-dimensional zirconia nanonet for direct indole synthesis, J. Am. Chem. Soc. 141 (2019) 10590–10594.

[30] Q. Deng, J. Lu, G. Sheng, Y.-C. Zhang, J. Wang, Z. Zeng, T. Yoskamtorn, S.C.E. Tsang, Catalytic hydrodehydroxylation of biomass-related chemicals via water-mediated hydrogen heterolysis over a Pd-S interface, ACS Catal. 13 (2023) 14356–14366.

[31] W. Zhang, Q. Qin, L. Dai, R. Qin, X. Zhao, X. Chen, D. Ou, J. Chen, T.T. Chuong, B. Wu, N. Zheng, Electrochemical reduction of carbon dioxide to methanol on hierarchical Pd/SnO$_2$ nanosheets with abundant Pd–O–Sn interfaces, Angew. Chem. Int. Ed. 57 (2018) 9475–9479.

[32] Z. Hou, L. Dai, J. Deng, G. Zhao, L. Jing, Y. Wang, X. Yu, R. Gao, X. Tian, H. Dai, D. Wang, Y. Liu, Electronically engineering water resistance in methane

combustion with an atomically dispersed tungsten on PdO catalyst, Angew. Chem. Int. 61 (2022), e202201655.

[33] M. Chia, Y.J. Pagán-Torres, D. Hibbitts, Q. Tan, H.N. Pham, A.K. Datye, M. Neurock, R.J. Davis, J.A. Dumesic, Selective hydrogenolysis of polyols and cyclic ethers over bifunctional surface sites on rhodium–rhenium catalysts, J. Am. Chem. Soc. 133 (2011) 12675–12689.

[34] S. Koso, Y. Nakagawa, K. Tomishige, Mechanism of the hydrogenolysis of ethers over silica-supported rhodium catalyst modified with rhenium oxide, J. Catal. 280 (2011) 221–229.

[35] S. Li, M. Dong, M. Peng, Q. Mei, Y. Wang, J. Yang, Y. Yang, B. Chen, S. Liu, D. Xiao, H. Liu, D. Ma, B. Han, Crystal-phase engineering of PdCu nanoalloys facilitates selective hydrodeoxygenation at room temperature, Innovation 3 (2022), 100189.

[36] S. Li, M. Dong, J. Yang, X. Cheng, X. Shen, S. Liu, Z.-Q. Wang, X.-Q. Gong, H. Liu, B. Han, Selective hydrogenation of 5-(hydroxymethyl) furfural to 5-methylfurfural over single atomic metals anchored on Nb$_2$O$_5$, Nat. Com. 12 (2021) 584.

[37] J. Chuseang, R. Nakwachara, M. Kalong, S. Ratchahat, W. Koo-amornpattana, W. Klysubun, P. Khemthong, K. Faungnawakij, S. Assabumrungrat, V. Itthibenchapong, A. Srifa, Selective hydrogenolysis of furfural into fuel additive 2-methylfuran over a rhenium-promoted copper catalyst, Sustain. Energy Fuels 5 (2021) 1379–1393.

[38] Y. Deng, R. Gao, L. Lin, T. Liu, X.-D. Wen, S. Wang, D. Ma, Solvent tunes the selectivity of hydrogenation reaction over α-MoC catalyst, J. Am. Chem. Soc. 140 (2018) 14481–14489.

[39] A.J. Kumalaputri, G. Bottari, P.M. Erne, H.J. Heeres, K. Barta, Tunable and selective conversion of 5-HMF to 2,5-furandimethanol and 2,5-dimethylfuran over copper doped porous metal oxides, ChemSusChem 7 (2014) 2266–2275.

[40] Q. Wang, Z. Yu, J. Feng, P. Fornasiero, Y. He, D. Li, Insight into the effect of dual active Cu^0/Cu$^+$ sites in a Cu/ZnO-Al$_2$O$_3$ catalyst on 5-hydroxylmethylfurfural hydrodeoxygenation, ACS Sus. Chem. Eng. 8 (2020) 15288–15298.

[41] L. Huang, L. Wang, Z. Zhang, X. Guo, X. Zhang, J.M. Chabu, P. Liu, F. Tang, Understanding the promotional effects of trace doped Zn in Co/NC for efficient one-pot catalytic conversion of furfural to 2-methyltetrahydrofuran, J. Energy Chem. 71 (2022) 225–233.

[42] Z. Zhang, Z. Pei, H. Chen, K. Chen, Z. Hou, X. Lu, P. Ouyang, J. Fu, Catalytic in-situ hydrogenation of furfural over bimetallic Cu-Ni alloy catalysts in isopropanol, Ind. Eng. Chem. Res. 57 (2018) 4225–4230.

[43] Z. Gao, C. Li, G. Fan, L. Yang, F. Li, Nitrogen-doped carbon-decorated copper catalyst for highly efficient transfer hydrogenolysis of 5-hydroxymethylfurfural to convertibly produce 2,5-dimethylfuran or 2,5-dimethyltetrahydrofuran, Appl. Catal. B 226 (2018) 523–533.

[44] S. Chen, C. Ciotonea, K.D.O. Vigier, F. Jérôme, R. Wojcieszak, F. Dumeignil, E. Marceau, S. Royer, Hydroconversion of 5-hydroxymethylfurfural to 2,5-dime-thylfuran and 2,5-dihydroxymethyltetrahydrofuran over non-promoted Ni/SBA-15, ChemCatChem 12 (2020) 2050–2059.

[45] G.-H. Wang, J. Hilgert, F.H. Richter, F. Wang, H.-J. Bongard, B. Spliethoff, C. Weidenthaler, F. Schüth, Platinum-cobalt bimetallic nanoparticles in hollow carbon nanospheres for hydrogenolysis of 5-hydroxymethylfurfural, Nature Mater. 13 (2014) 293–300.

[46] N. Viar, J.M. Requies, I. Agirre, A. Iriondo, M. Gil-Calvo, P.L. Arias, Ni–Cu bimetallic catalytic system for producing 5-hydroxymethylfurfural-derived value-added biofuels, ACS Sus. Chem. Eng. 8 (2020) 11183–11193.

[47] Q. Deng, R. Gao, X. Li, J. Wang, Z. Zeng, J.-J. Zou, S. Deng, Hydrogenative ring-rearrangement of biobased furanic aldehydes to cyclopentanone compounds over Pd/pyrochlore by introducing oxygen vacancies, ACS Catal. 10 (2020) 7355–7366.

[48] Z. Tong, X. Li, J. Dong, R. Gao, Q. Deng, J. Wang, Z. Zeng, J.-J. Zou, S. Deng, Adsorption configuration-determined selective hydrogenative ring opening and ring rearrangement of furfural over metal phosphate, ACS Catal. 11 (2021) 6406–6415.

[49] L. Zhang, Y. Zhong, J. Wang, Z. Zeng, S. Deng, J.-J. Zou, Q. Deng, Intermetallic palladium-zinc nanoparticles for the ultraselective hydrogenative rearrangement of furan compounds, ACS Catal. 13 (2023) 13205–13214.

[50] Q. Deng, X. Li, R. Gao, J. Wang, Z. Zeng, J.-J. Zou, S. Deng, S.C.E. Tsang, Hydrogen-catalyzed acid transformation for the hydration of alkenes and epoxy alkanes over Co-N frustrated lewis pair surfaces, J. Am. Chem. Soc. 143 (2021) 21294–21301.

[51] W.H.K. Ng, E.S. Gnanakumar, E. Batyrev, S.K. Sharma, P.K. Pujari, H.F. Greer, W. Zhou, R. Sakidja, G. Rothenberg, M.W. Barsoum, N.R. Shiju, The Ti$_3$AlC$_2$ MAX phase as an efficient catalyst for oxidative dehydrogenation of n-butane, Angew. Chem. Int. Ed. 57 (2018) 1485–1490.

[52] P. Liu, Y. Zhao, R. Qin, S. Mo, G. Chen, L. Gu, D.M. Chevrier, P. Zhang, Q. Guo, D. Zang, B. Wu, G. Fu, N. Zheng, Photochemical route for synthesizing atomically dispersed palladium catalysts, Science 352 (2016) 797–800.

[53] D. Yang, H. Liu, D.-L. Wang, Z. Luo, Y. Lu, F. Xia, Y. Liu, Co-catalysis over a bi-functional ligand-based Pd-catalyst for tandem bis-alkoxycarbonylation of terminal alkynes, Green. Chem. 20 (2018) 2588–2595.

[54] A.H. Mamaghani, F. Haghighat, C.-S. Lee, Gas phase adsorption of volatile organic compounds onto titanium dioxide photocatalysts, Chem. Eng. J. 337 (2018) 60–73.

[55] B. Chen, C.W. Kirby, Y. Huang, Investigation of crystallization of molecular sieve AlPO$_4$-5 by the dry gel conversion method, J. Phys. Chem. C 113 (2009) 15868–15876.

[56] S.H. Alahakoon, M.J. Willans, Y. Huang, In situ multinuclear magic-angle spinning NMR: monitoring crystallization of molecular sieve AlPO$_4$-11 in real time, JACS Au 3 (2023) 1670–1683.

[57] C. Zhao, Y. Kou, A.A. Lemonidou, X. Li, J.A. Lercher, Highly selective catalytic conversion of phenolic bio-oil to alkanes, Angew. Chem. Int. Ed. 48 (2009) 3987–3990.

[58] Y. Liang, H. Wang, H. Xin, X. Hu, L. Yan, Q. Zhang, C. Wang, Q. Liu, L. Ma, Selective cellulose hydrogenolysis to 2,5-hexanedione and 1-hydroxy-2-hexanone using Ni@NC combined with H$_3$PO$_4$, ACS Sus. Chem. Eng. 9 (2021) 15394–15405.

[59] C. Emeis, Determination of integrated molar extinction coefficients for infrared absorption bands of pyridine adsorbed on solid acid catalysts, J. Catal. 141 (1993) 347–354.

[60] L. Dong, J. Morales-Vidal, L. Mu, L. Li, N. López, J. Pérez-Ramírez, Z. Chen, Selective hydrogenolysis of 5-hydroxymethylfurfural to 5-methylfurfural over Au/TiO$_2$, Appl. Catal. B 335 (2023), 122893.

[61] H. Ishikawa, M. Sheng, A. Nakata, K. Nakajima, S. Yamazoe, J. Yamasaki, S. Yamaguchi, T. Mizugaki, T. Mitsudome, Air-stable and reusable cobalt phosphide nanoalloy catalyst for selective hydrogenation of furfural derivatives, ACS Catal. 11 (2021) 750–757.